Supporting Information for: Atomistic Hydrodynamics and the Dynamical Hydrophobic Effect in Porous Graphene

Steven E. Strong and Joel D. Eaves*
Department of Chemistry and Biochemistry, University of Colorado, Boulder, Colorado, United States
(Dated: May 5, 2016)

CONTENTS

* Joel.Eaves@colorado.edu

I. DERIVATION OF GAUSSIAN DYNAMICS

Here we derive Eq. 3 in the main text, and show that the flow, temperature, and geometry constraints separate completely. Consider a system of N particles with masses $\{m\}$ at positions $\{\mathbf{r}\}$. We follow the prescription for Gauss's principal of least constraint found in Ref. [1]. In the main text, we discuss the "Evans-Morriss" constraint, G_{EM} [1–6]. Here, we split this into its two components, the temperature constraint, G_{T}, and the geometry (molecular) constraint, G_{m}. The Gaussian cost function is

$$C\big(\{\ddot{\mathbf{r}}\}\big) = \frac{1}{2}\sum_{i=1}^{N} m_i\left(\ddot{\mathbf{r}}_i - \frac{\mathbf{F}_i}{m_i}\right)^2 + \lambda_{\mathrm{T}} G_{\mathrm{T}} + \lambda_{\mathrm{m}} G_{\mathrm{m}} + \boldsymbol{\lambda}_{\mathrm{f}} \cdot \mathbf{G}_{\mathrm{f}}, \tag{1}$$

where m_i is the mass of the i-th particle and $\mathbf{F}_i$ is the total force on the i-th particle. We use a dot to indicate a time derivative. The λs are the Gaussian multipliers. We could treat the geometry constraint explicitly here, but it is well known, and its use in conjunction with a temperature constraint is also well known [5–8]. Here, we need only show that the solutions for $\boldsymbol{\lambda}_{\mathrm{f}}$ and λ_{m} separate completely. This is apparent from the result (Eq. 13), which shows that the flow constraint applies a uniform acceleration to all particles. It is clear that a uniform acceleration cannot distort any bonds or angles. So, from here on out, we only consider $\mathbf{G}_{\mathrm{f}}$ and G_{T}.

A capital G denotes the form of the constraint that depends on the accelerations. These are derived from the physically motivated constraints, g,

$$g_{\mathrm{T}}\big(\{\mathbf{r}, \dot{\mathbf{r}}\}\big) = \sum_{i=1}^{N} \frac{1}{2} m_i \big(\dot{\mathbf{r}}_i - \mathbf{u}(\mathbf{r}_i)\big)^2 - \frac{3}{2} N k_B T = 0 \tag{2}$$

$$\mathbf{g}_{\mathrm{f}}\big(\{\mathbf{r}, \dot{\mathbf{r}}\}\big) = \sum_{i=1}^{N} m_i \big(\dot{\mathbf{r}}_i - \mathbf{u}(\mathbf{r}_i)\big) = 0, \tag{3}$$

where $\mathbf{u}(\mathbf{r})$ is the local streaming velocity of the fluid, k_B is Boltzmann's constant, and T is the temperature. Equation 2 is an isokinetic thermostat, but can easily be generalized to a Nosé-Hoover thermostat [1], which is what we use in our simulations. Equation 3 is the flow constraint. These are both nonholonomic constraints, since they depend on the velocities, so to find the functions G we take one time derivative:

$$G_T = \frac{\partial}{\partial t} g_{\mathrm{T}} = \sum_{i=1}^{N} m_i \big(\dot{\mathbf{r}}_i - \mathbf{u}(\mathbf{r}_i)\big) \cdot \ddot{\mathbf{r}}_i = 0 \tag{4}$$

$$\mathbf{G}_{\mathrm{f}} = \frac{\partial}{\partial t} \mathbf{g}_{\mathrm{f}} = \sum_{i=1}^{N} m_i \ddot{\mathbf{r}}_i = 0. \tag{5}$$

We have used the fact that at steady state, the streaming velocity is time-independent. The Gaussian cost function is now

$$C\big(\{\ddot{\mathbf{r}}\}\big) = \frac{1}{2}\sum_{i=1}^{N} m_i\left(\ddot{\mathbf{r}}_i - \frac{\mathbf{F}_i}{m_i}\right)^2 + \lambda_{\mathrm{T}} \sum_{i=1}^{N} m_i \big(\dot{\mathbf{r}}_i - \mathbf{u}(\mathbf{r}_i)\big) \cdot \ddot{\mathbf{r}}_i + \boldsymbol{\lambda}_{\mathrm{f}} \cdot \sum_{i=1}^{N} m_i \ddot{\mathbf{r}}_i. \tag{6}$$

We find the accelerations that minimize this cost function:

$$\frac{\partial}{\partial \ddot{\mathbf{r}}_i} C\big(\{\ddot{\mathbf{r}}\}\big) = m_i \left(\ddot{\mathbf{r}}_i - \frac{\mathbf{F}_i}{m_i}\right) + \lambda_{\mathrm{T}} m_i \big(\dot{\mathbf{r}}_i - \mathbf{u}(\mathbf{r}_i)\big) + \boldsymbol{\lambda}_{\mathrm{f}} m_i = 0. \tag{7}$$

This gives the equation of motion

$$m_i \ddot{\mathbf{r}}_i = \mathbf{F}_i - \lambda_{\mathrm{T}} m_i \big(\dot{\mathbf{r}}_i - \mathbf{u}(\mathbf{r}_i)\big) - \boldsymbol{\lambda}_{\mathrm{f}} m_i. \tag{8}$$

To solve for the temperature multiplier, λ_{T}, we take the scalar product of Eq. 8 with $\big(\dot{\mathbf{r}}_i - \mathbf{u}(\mathbf{r}_i)\big)$, and then sum over all particles:

$$\sum_{i=1}^{N} m_i \big(\dot{\mathbf{r}}_i - \mathbf{u}(\mathbf{r}_i)\big) \cdot \ddot{\mathbf{r}}_i = \sum_{i=1}^{N} \big(\dot{\mathbf{r}}_i - \mathbf{u}(\mathbf{r}_i)\big) \cdot \mathbf{F}_i - \lambda_{\mathrm{T}} \sum_{i=1}^{N} m_i \big(\dot{\mathbf{r}}_i - \mathbf{u}(\mathbf{r}_i)\big)^2 - \boldsymbol{\lambda}_{\mathrm{f}} \sum_{i=1}^{N} m_i \big(\dot{\mathbf{r}}_i - \mathbf{u}(\mathbf{r}_i)\big). \tag{9}$$

The term on the left hand side is zero, due to Eq. 4, and the $\boldsymbol{\lambda}_\mathrm{f}$ term on the right is zero due to Eq. 3. We can now solve for λ_T, and the result is

$$\lambda_\mathrm{T} = \frac{\sum_{i=1}^{N} \left(\dot{\mathbf{r}}_i - \mathbf{u}(\mathbf{r}_i)\right) \cdot \mathbf{F}_i}{\sum_{i=1}^{N} m_i \left(\dot{\mathbf{r}}_i - \mathbf{u}(\mathbf{r}_i)\right)^2}. \tag{10}$$

This is the well known result for the Gaussian isokinetic thermostat [1–4]. It is profile-unbiased, meaning that it is applied on the peculiar velocities of the system, with the local streaming velocity removed [9].

We now solve for the flow multiplier, $\boldsymbol{\lambda}_\mathrm{f}$, by summing Eq. 8 over all particles:

$$\sum_{i=1}^{N} m_i \ddot{\mathbf{r}}_i = \sum_{i=1}^{N} \mathbf{F}_i - \lambda_\mathrm{T} \sum_{i=1}^{N} m_i \left(\dot{\mathbf{r}}_i - \mathbf{u}(\mathbf{r}_i)\right) - \boldsymbol{\lambda}_\mathrm{f} \sum_{i=1}^{N} m_i. \tag{11}$$

The term on the left hand side is zero due to Eq. 5, and the λ_T term on the right hand side is zero due to Eq. 3. So, we can solve for $\boldsymbol{\lambda}_\mathrm{f}$:

$$\boldsymbol{\lambda}_\mathrm{f} = \frac{1}{M} \sum_{i=1}^{N} \mathbf{F}_i, \tag{12}$$

where we have defined $M \equiv \sum_{i=1}^{N} m_i$ as the total mass of the system. The resulting equation of motion is

$$m_i \ddot{\mathbf{r}}_i = \mathbf{F}_i - m_i \mathbf{I} - m_i \xi (\dot{\mathbf{r}}_i - \mathbf{u}(\mathbf{r}_i)), \tag{13}$$

where we have made the definitions

$$\mathbf{I} \equiv \boldsymbol{\lambda}_\mathrm{f} = \frac{1}{M} \sum_{i=1}^{N} \mathbf{F}_i, \tag{14}$$

$$\xi \equiv \lambda_\mathrm{T} = \frac{\sum_{i=1}^{N} \left(\dot{\mathbf{r}}_i - \mathbf{u}(\mathbf{r}_i)\right) \cdot \mathbf{F}_i}{\sum_{i=1}^{N} m_i \left(\dot{\mathbf{r}}_i - \mathbf{u}(\mathbf{r}_i)\right)^2}. \tag{15}$$

Including the geometry constraints would simply add another term to the equation, $\mathbf{f}_i$ [1, 5, 6]:

$$m_i \ddot{\mathbf{r}}_i = \mathbf{F}_i - m_i \mathbf{I} - m_i \xi (\dot{\mathbf{r}}_i - \mathbf{u}(\mathbf{r}_i)) + \mathbf{f}_i, \tag{16}$$

We were able to solve for the temperature and flow Gaussian multipliers independently, so we have shown that these constraints separate completely. We argued that the geometry constraint separates because the uniform acceleration applied by the flow constraint cannot change any relative geometries.

a. *Properties of the Applied Field,* $\mathbf{I}$

The applied acceleration field $\mathbf{I}$ is fluctuating and weak. For reference, at the Reynolds numbers we discuss in the main text, the average applied force on a single particle is on the order of the force between two Lennard-Jones particles separated by 3 σ. The fluctuations have a standard deviation that is on the order of twice the mean. The exact quantities depend on the particular simulation geometry and flow rate.

II. HAGEN-POISEUILLE LAW

a. *Assumptions*

The Hagen-Poiseuille (HP) law assumes the following: [10–13]:

1. The fluid is incompressible.
2. The flow is at low Re.

3. The flow is at steady state.
4. The fluid is Newtonian.
5. The fluid acts as a continuum.
6. There is no-slip at the walls.
7. The channel is long enough that the flow profile is well developed.

Some of these are good assumptions:

1. The fluid is relatively incompressible; the density only changes by a few percent in our simulations (§ VII).
2. We are at low enough Re that the flow is not turbulent (Re $\lesssim 10$).
3. We ensure steady-state as discussed in § V.

But some are bad assumptions:

4. Lennard-Jones fluids are Newtonian at low shear rates, but non-Newtonian at high shear rates. We do not know where our 2D system falls in this regime [14–16].
5. An atomic system is not a continuum.
6. No-slip boundary conditions are impossible in an atomic simulation.
7. The channels are at most 100 σ long: very short relative to the engineering applications for which the HP law was intended.

Clearly, we would not expect the HP law to hold in this application; if it were quantitative, all the points in Fig. 1d in the main text would lie on the same point. However, it does provide a means by which to compare the relationship of the flux to the pressure drop for a variety of channel geometries. Note that in Fig. 1d in the main text, the effective viscosity appears to be converging to some value as Re increases. This is probably because Re is proportional to L, and as L increases, the HP law becomes more accurate. This is not meaningful, since we are not interested in quantitative accuracy of the HP law.

b. Derivation of Hagen-Poiseuille law in 2D

We now derive the HP law in 2D for the channel geometry shown in Fig. 1a in the main text. The continuity equation is

$$\frac{\partial \rho(\mathbf{r},t)}{\partial t} + \boldsymbol{\nabla} \cdot \mathbf{J}(\mathbf{r},t) = 0. \tag{17}$$

Both the assumptions of steady state and incompressibility give

$$\frac{\partial \rho(\mathbf{r},t)}{\partial t} = 0. \tag{18}$$

Equations 17 and 18 combine to give

$$\frac{\partial u_x}{\partial x} + \frac{\partial u_y}{\partial y} = 0, \tag{19}$$

where u_x and u_y are the components of the velocity field. We know that $u_y = 0$, so $\partial u_y/\partial y = 0$, and therefore $\partial u_x/\partial x = 0$ as well. The Navier-Stokes equation for an incompressible fluid at low Reynolds number is

$$\rho \frac{\partial \mathbf{u}}{\partial t} = -\boldsymbol{\nabla} P + \rho \mathbf{g} + \eta \boldsymbol{\nabla}^2 \mathbf{u}. \tag{20}$$

From here on out, we ignore the gravity term. Since the flow is at steady state, $\partial \mathbf{u}/\partial t = 0$, so the left-hand-side of the equation is zero. There is only a pressure drop along the direction of flow, so only the x-component of $\boldsymbol{\nabla} P$ is non-zero. The x-component of Eq. 20 is

$$\frac{\partial P}{\partial x} = \eta \left(\frac{\partial^2 u_x}{\partial x^2} + \frac{\partial^2 u_x}{\partial y^2} \right) \tag{21}$$

$$= \eta \frac{\partial^2 u_x}{\partial y^2}, \tag{22}$$

where we used the fact that $\partial u_x/\partial x = 0$. Since u_x is not a function of x, we can easily integrate both sides with respect to x:

$$P(x) = c_1 x + c_2. \tag{23}$$

We now use the boundary conditions at the ends of the channel: $P(0) = P_1$ and $P(L) = P_2$, with $\Delta P \equiv P_1 - P_2$,

$$P(x) = P_1 - \frac{\Delta P}{L} x. \tag{24}$$

We now plug this back in to Eq. (22):

$$-\frac{\Delta P}{\eta L} = \frac{\partial^2 u_x}{\partial y^2}. \tag{25}$$

We integrate both sides of the equation with respect to y twice:

$$u_x(y) = -\frac{\Delta P}{2\eta L} y^2 + k_1 y + k_2. \tag{26}$$

We use no-slip boundary conditions: $u_x(-d/2) = u_x(d/2) = 0$:

$$u_x(y) = \frac{\Delta P}{2\eta L}\left[\left(\frac{d}{2}\right)^2 - y^2\right]. \tag{27}$$

To get the flow rate, Q, we integrate the product of the density and the velocity profile over the width of the pore. For an incompressible fluid, the density is not a function of y:

$$Q \equiv \rho \int_{-d/2}^{d/2} u_x(y) dy \tag{28}$$

$$= \rho \int_{-d/2}^{d/2} \frac{\Delta P}{2\eta L}\left[\left(\frac{d}{2}\right)^2 - y^2\right] dy \tag{29}$$

$$= \frac{\Delta P \rho d^3}{12\eta L}. \tag{30}$$

We can now define the mass flux, J, as the flow rate through a cross-sectional area (length in 2D),

$$J = \frac{Q}{d}. \tag{31}$$

The result is

$$J = \frac{\Delta P \rho d^2}{12\eta L}. \tag{32}$$

This is the Hagen-Poiseuille law in 2D. Note that it is identical to the Hagen-Poiseuille law in 3D [13]. This would not be the case if we expressed it in terms of Q instead of J; normalization by the cross-sectional area/length is different in 2D/3D.

III. HYDROSTATIC CORRECTION TO THE PRESSURE PROFILE

The applied force in GD, $m_i\mathbf{I}$, fluctuates, but has a non-zero mean. So, there is an overall uniform applied force, which induces a hydrostatic pressure gradient. The GD pressure profile is the sum of the hydrostatic part and the pressure drop part, resulting from the presence of the channel (Fig. 1),

$$P(x) = P_{\text{drop}}(x) + P_{\text{hydrostatic}}(x). \tag{33}$$

In all of our calculations here, we use only the pressure drop part of the profile (P_{drop}), which we calculate by removing the theoretical hydrostatic gradient that is induced by the applied acceleration,

$$P_{\text{hydrostatic}}(x) = -\overline{I_x}\rho(x)x. \tag{34}$$

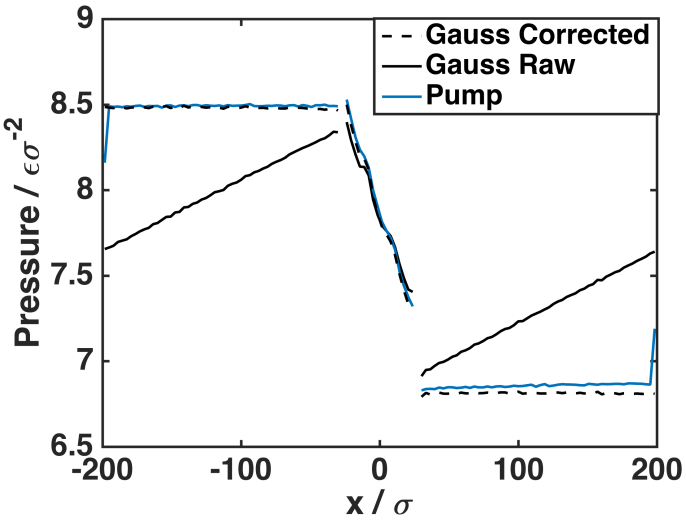

FIG. 1. Representative pressure profiles from GD (black) and the pump method (blue). The solid lines show the raw data from the simulations. The pressure profile in the pump method is flat on both sides of the channel, while the pressure profile in GD is linearly increasing due to the hydrostatic part. We remove the hydrostatic part to get the pressure drop purely due to the channel (dashed black line), as discussed in the text. The gaps in the profiles are at the edges of the channel, where the pressure is poorly defined because the length of the channel is poorly defined.

Here, $\overline{I_x}$ is the time average of the applied acceleration in the x-direction, and $\rho(x)$ is the mass density profile of the fluid. This density is computed using the volume that the fluid occupies, not the full volume of the simulation box, such that

$$\frac{1}{L_x}\int_{-L_x/2}^{L_x/2}\rho(x)\,dx = \rho_0. \tag{35}$$

Note that the ρ_0 used here is the same as the ρ used in the main text. This is done to distinguish ρ_0 from $\rho(x)$.

IV. EFFECTIVE VISCOSITY CALCULATION

The calculation of the effective viscosity in the 2D simulations is done in several steps: 1) calculate the pressure drop, 2) calculate the flux, and 3) fit these points to a line to estimate the slope of ΔP versus J.

a. Pressure Drop

The pressure drop is calculated as follows:

1. Bootstrap over the 96 trials (§ IX).
2. Average the pressure profile over each bootstrap sample.
3. For each averaged profile, fit two lines to the flat parts of the profile.
4. Extrapolate these lines to the edges of the pore, as defined by L, from Eq. 53 (or Eq. 55 for the water-graphene simulations).
5. The pressure drop is the difference between these extrapolated values.
6. The mean is the average of the bootstrap samples. The standard error is the standard deviation of the bootstrap samples, multiplied by $\sqrt{N_{\text{trial}}}$, where N_{trial} is the number of trials (96).

This procedure is used because each of the 96 individual pressure profiles are too noisy to reliably fit and calculate a pressure drop independently, so an averaged pressure drop must be used. However, if one simply averages all the pressure profiles, and uses a point-by-point standard deviation of the pressure profile to estimate the error of the pressure drop, the error is deceptively low. This is because the fitting procedure masks the variation between trials. We use the bootstrap procedure so that we can fit to an averaged pressure profile, but still retain information about the variation between trials.

b. Flux

The mass flux is defined as

$$\mathbf{J} = \rho_{\mathrm{t}}\mathbf{u}, \tag{36}$$

where $\mathbf{u}$ is the total center-of-mass velocity, and ρ_{t} is the *total* density of the fluid in the simulation,

$$\rho_{\mathrm{t}} = \frac{N}{L_x L_y}. \tag{37}$$

Note that N is the number of fluid particles only and does not include the wall particles. Also, $L_x L_y$ is the area of the *entire* simulation box, and does not account for the excluded area due to the channel. So, ρ_{t} is *not* equal to the bulk fluid density, ρ_0; ρ_{t} is related to ρ_0 via the dimensions of the channel and simulation box. Note that the ρ_0 used here is the same as the ρ used in the main text. This is done to distinguish ρ_0 from $\rho(x)$. We always use the magnitude of the flux vector, $J = |\mathbf{J}|$, and in practice, since the only significant flux is in the x-direction, we calculate the flux using

$$J = J_x = \rho_{\mathrm{t}} u_x, \tag{38}$$

with

$$u_x = \frac{\sum_{i=1}^{N} m_i v_{x,i}}{\sum_{i=1}^{N} m_i}, \tag{39}$$

where $v_{x,i}$ is the velocity of the i-th particle in the x-direction. We calculate the flux mean and error as a simple mean and standard deviation over the 96 trials.

c. Slope

For each channel geometry, we performed simulations at three different fluxes. At each of these three data points, we have a value of J and ΔP, and associated errors. We calculate the average slope by simply finding the least-squares estimate for the slope; the intercept of the line is fixed to zero. We calculate the error on the slope by finding the least-squares fits for the data plus and minus their respective error. This is best illustrated by the following equations, where we use an underbar to denote the vectors of data that contain the three data points at varying fluxes:

$$\underline{J} m = \underline{\Delta P} \tag{40}$$

$$(\underline{J} + \underline{\sigma}_J) m_- = (\underline{\Delta P} - \underline{\sigma}_{\Delta P}) \tag{41}$$

$$(\underline{J} - \underline{\sigma}_J) m_+ = (\underline{\Delta P} + \underline{\sigma}_{\Delta P}). \tag{42}$$

We solve these linear equations for the least-squares slope, m, and the error, m_- and m_+. Using Eq. 5 in the main text, the effective viscosity is

$$\eta_{\mathrm{eff}} = \frac{d^2 \rho}{12 L} m. \tag{43}$$

V. CONVERGENCE AND VALIDATION OF SIMULATIONS

The nonequilibrium simulations must be validated in two ways. First, the simulations must be at steady state. The continuity equation for fluid dynamics,

$$\frac{\partial \rho(\mathbf{r}, t)}{\partial t} + \boldsymbol{\nabla} \cdot \mathbf{J}(\mathbf{r}, t) = 0, \tag{44}$$

says that at steady state, the flux profile is flat. So, we verify that our simulations are at steady state by testing that the flux profile is flat within noise.

Second, we must verify that the reservoirs on each side of the channel are large enough. Here, "large enough" means that once a particle exits the channel, diffusive motion should dissipate the high velocity before the particle wraps

back around to the channel again. We run simulations at varying box lengths and look for convergence of the effective viscosity. This is not as straight-forward as it sounds, because longer boxes require longer time to reach steady state. This is because the density profile is longer ranged and requires more time to develop. So, one must simultaneously increase the box length and make sure that the simulations are still at steady state.

Due to computation time, this is not feasible in the water simulations. Instead we performed a few simulations at twice the box length, and found no changes in the results.

VI. MODIFIED PUMP METHOD AND STANDARD ERRORS

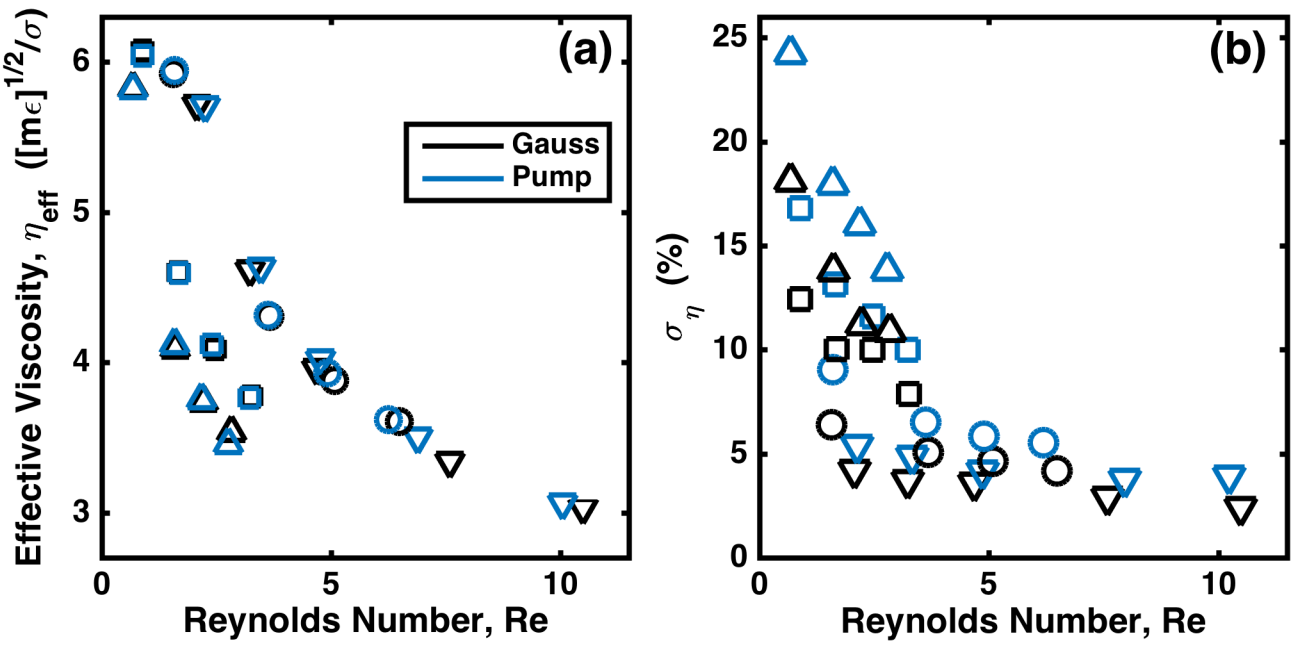

FIG. 2. Panel (a) shows the effective viscosity calculated with the pump method modified to use a profile-unbiased thermostat. This figure looks almost identical to Fig. 1d in the main text. The agreement between the two methods is better at Re > 5, but there is still disagreement, especially for the narrowest channel ($\bigtriangledown$). Panel (b) shows the relative error on the values of the effective viscosity plotted in Fig. 1d in the main text. For a given channel diameter (symbol shape), Gaussian dynamics always has smaller error than the pump method. The symbols used here correspond to channel diameter in the same way as described in Fig. 1d in the main text.

VII. DENSITY PROFILE

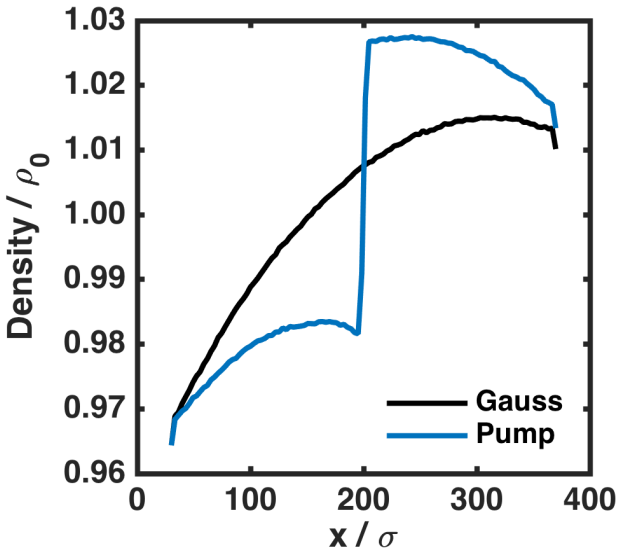

FIG. 3. The density profiles for the pump method and GD are shown in blue and black, respectively. This is the same figure as shown inset in Fig. 1c in the main text. The purpose of this figure is to clarify which part of the simulation box is shown here. This plot is centred around the edge of the box, i.e., the pump region, not the pore. The pore is centred at $x = 0\ \sigma$, and there is a periodic replica of the pore at $x = 400\ \sigma$. The density profile for the pump method is discontinuous in the pump region, and this represents a disadvantage of that method (§ XII). The density profile inside the pore is not shown, because the density is higher inside the pore and is off the scale of this plot.

VIII. PERMEABILITY CALCULATIONS

The calculation of the permeability in the water-graphene simulations is similar to the calculation of the effective viscosity in the 2D Lennard-Jones calculations. The permeability serves the same purpose as the effective viscosity: to compare the results of different calculations. The permeability is a more intuitive quantity than the effective viscosity, but the effective viscosity "normalizes" for different size channels. The 2D simulations involve channels which vary significantly in size. Clearly the permeability of a channel which is 18 σ wide will be much larger than the permeability of a channel which is 4 σ wide. In the water-graphene simulations, however, we only consider one size channel, so we can use the more intuitive permeability. Here, we follow the discussion in Ref. [17]. The osmotic permeability is defined as

$$q_n = p\Delta C, \tag{45}$$

where q_n is the molar flow rate of water (mol/time), p is the osmotic permeability (volume/time), and ΔC is the solute concentration difference (mol/volume). We can now use the Van't Hoff equation,

$$\Delta P = k_B T N_A \Delta C, \tag{46}$$

where k_B is Boltzmann's constant, T is the temperature, N_A is Avogadro's number, and ΔP is the osmotic pressure drop. Equations 45 and 46 yield

$$p = k_B T N_A \frac{q_n}{\Delta P}. \tag{47}$$

So, to calculate the permeability, we need to measure the flux (or flow rate) and the pressure drop in the simulations. Note that this nonequilibrium formulation does not require knowledge of the volume of a single water molecule, unlike the procedure described in Ref. [17]. Also note that the sign of this equation trivially depends on whether the pressure drop is defined as a positive or negative quantity. We can define a molecular flux (molecules/time) to replace the molar flux,

$$q = q_n N_A. \tag{48}$$

The permeability is

$$p = k_B T \frac{q}{\Delta P}. \tag{49}$$

We calculate the pressure drop and flux as described in § IV. Because these simulations are more expensive than the 2D simulations, we only perform simulations at two different flow rates for each applied voltage. We calculate the slope of q vs. ΔP using the same procedure as § IV c. Note, however, that this is the inverse of the slope used in § IV c. We then use Eq. 49 to calculate the permeability.

a. Steady State

The fluxes involved in these simulations are much smaller than those in the 2D simulations; the Reynolds number for the water-graphene flow is about 0.001 (§ XI). Because the flow is so slow, the flux profile is too noisy to determine whether the simulations are at steady state. So, to test for steady state, we compare the global flux ($\mathbf{J} = \rho_t \mathbf{u}$) to a measure of the local flux inside the pore. The local flux is measured by counting the number of net passage events through the pore, using the collective variable defined in Ref. [17] (Eq. 51). This gives a molecular flow rate, q, which can be converted to a flux using

$$J = \frac{q M_R}{N_A L_y L_z}, \tag{50}$$

where M_R is the molar mass of water, N_A is the Avogadro constant, and L_y and L_z are the dimensions of the simulation box perpendicular to the flow.

b. Equilibrium Method

We also calculate the permeability using an equilibrium linear response method, developed in Ref. [17]. This method uses a collective variable $n(t)$. The definition of $n(t)$ and the derivation of the method can be found in Ref. [17]. We also use the collective variable $n(t)$ to calculate the local flux, as discussed above. At steady state, $n(t)$ is linearly increasing, and the slope is equal to the flow rate [17],

$$q = \frac{\langle n(t) \rangle}{t}. \tag{51}$$

We estimate q by fitting $n(t)$ to a line.

IX. SIMULATION DETAILS

In the pump method, the pressure drop is given by the total force applied to the simulation divided by the cross-sectional area (length in 2D) over which it is applied:

$$\Delta P = \frac{F}{A}. \tag{52}$$

In 2D, $A = L_y$, and in 3D, $A = L_y L_z$, where the flow is in the x-direction. Since A is constant, in order to fix the pressure drop, the total force on the simulation is also constant [18, 19]. The number of particles in the pump region fluctuations, so the force on each particle fluctuates by a small amount.

In GD, the fluid is initially given a uniformly distributed center-of-mass momentum. The GD constraint simply keeps the total center-of-mass momentum fixed, allowing the flow profile to relax into a natural one.

a. Two-Dimensional Lennard-Jones Simulations

The Lennard-Jones particles have $\sigma = 1$ and $\epsilon = 1$. The interactions between the fluid particles are cutoff at 2.5 σ; the fluid-wall interactions are cutoff at $2^{1/6}\sigma$ [20–22]. The bulk fluid density is 0.8 σ^{-2}. The lattice spacing between wall particles is 1 σ. We use a timestep of 0.001 τ. The simulations are equilibrated for 10 τ at equilibrium, and then run for another 1000 τ to achieve a nonequilibrium steady state. We then collect data for 1000 τ. We average results over 96 trials. Some of the especially long and skinny channels require longer time to reach steady state (see Table I). The simulation box is usually 400×40 σ^2, where the flow is along the first dimension (x). In cases with longer channels, sometimes longer boxes are required to ensure that the results are converged with respect to the box length (see Table I). The center of the channel is located at the center of the box. The temperature is thermostatted at 2 ϵ/k_B using a Nosé-Hoover thermostat [7, 8] with a 0.1 τ damping time. With Gaussian dynamics (GD), we use a profile-unbiased thermostat with bins that contain an average of 8 particles [9]. With the pump method, the thermostat does not correct for the flow profile, because this is how the method is usually implemented [18, 19, 23–26]. In our simulations, the pump region is 5 σ thick and is centered at the box edge.

We account for the excluded volume of the wall particles when we define the size of the channel:

$$L = L_c + 2^{1/6}\sigma \tag{53}$$

$$d = d_c - 2^{1/6}\sigma, \tag{54}$$

where L is the length of the channel in the direction of the flow, d is the width of the channel, and the subscript c indicates the distance measured from center to center of wall particles.

b. Water-Graphene Simulations

We use the SPC/E water model [27], with the bonds and angles held rigid using the SHAKE algorithm [28]. The geometry of the pore in the graphene sheet is the same as the smaller of the two pores used by Suk and Aluru [29]. An image of the pore from our simulations can be seen in Fig. 4. The graphene-water potential is case 28 in Table 2 of Ref. [30]. This is the same potential that was used in Ref. [31], which showed that the hydrophobicity of graphene is tunable. This potential reproduces the wetting angle of water on graphite ($\sim 90^\circ$), although now there is evidence that the wetting angle of water on graphene is significantly higher [32].

TABLE I. The exceptions to the general procedure presented in § IX, for especially long and/or skinny channels. The variables L_c and d_c are defined in the text. L_x is the length of the simulation box in the direction of the flow.

L_c (σ)	d_c (σ)	Time to reach steady state (τ)	L_x (σ)
70	6	3000	600
70	10	1000	500
70	20	1000	500
80	16	1000	600
90	10	1000	600
90	20	1000	600

We first equilibrate a block of water at 298 K and 1 atm using a Nosé-Hoover thermostat [7, 8] and barostat [33] for 200 ps, with damping times of 0.2 ps and 2 ps, respectively. We then introduce the porous graphene sheet, and equilibrate again for 200 ps, while barostatting only in the dimension perpendicular to the graphene sheet. During this equilibration, we calculate the average box length. We then turn the barostat off and linearly scale the box length to its average for 100 ps. We then fix the box size and run for 2 ns to achieve a nonequilibrium steady state. During all nonequilibrium simulations, we use a profile-unbiased thermostat with bins that contain 4 water molecules on average [9]. We then collect data for 5 ns. We average results over 96 trials. The timestep is 2 fs. The simulation box is about $69 \times 37 \times 30$ Å^3, where the flow is along the first dimension. The length of the box in the direction of flow is not same in each trial due to the constant pressure equilibration steps. The box contains over 2000 water molecules. The coulomb interactions are computed using the PPPM method [34], optimized by the simulation package so that the forces are accurate to one part in one million [35]. In the pump method, the pump region is 8 Å thick and is centered at the edge of the simulation box. The force applied in the pump method is mass-weighted, so that no torque is applied to the molecules, and so that the rigidity of the molecules is maintained.

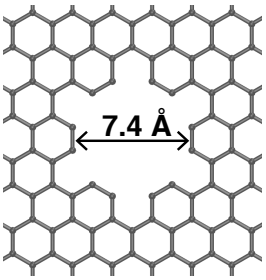

FIG. 4. The geometry of the pore in the graphene sheet, generated by removing all carbon atoms within a 3 Å radius of the center of a hexagonal cell.

In order to calculate the pressure drop (§ IV a), we need to define the "length" of the pore. We define the edge of the channel as the point where the density of water first reaches the average density within the pore. The length of the pore is then defined as the distance between this point on either side of the pore. This works out to

$$L = 3.8 \text{ Å}. \tag{55}$$

In the equilibrium simulations, we follow the same scheme as for the nonequilibrium simulations, except that we do not need to achieve steady state. We collect data for 5 ns. We average results over 96 trials.

We apply a voltage to the graphene sheet using the procedure described in [31]. The excess charge per carbon atom, q, is

$$q = -aV^2 \operatorname{sgn}(V), \tag{56}$$

where the constant $a = 0.019336\ e/\text{volt}^2$ [31].

X. MARKOV MODEL

We define the states of the Markov model by drawing a box on both sides of the pore (Fig. 5); when an oxygen atom is inside a box, that box is occupied. The Markov states are defined using the occupation of these boxes: the "full" state corresponds to both boxes being occupied, etc (see Fig. 3a in the main text). Since the length of the pore is 3.8 Å (Eq. 55), each box extends 1.9 Å from the sheet (Fig. 5). The size of the boxes in the other dimensions is irrelevant, because it is exceedingly rare for a molecule to come that close to the sheet if it is not inside the pore. Since our Markov model assumes that each box can only be singly occupied or empty, the boxes must be small enough so that double occupation is rare. Using boxes defined as described, the boxes are doubly occupied less than 0.3% of the time.

We compute the Markov transition probabilities by simply counting the number of transitions between each state and normalizing by the total number of transitions [36]. We calculate the steady-state populations of the Markov process by diagonalizing the transition probability matrix and finding the eigenvector with unit eigenvalue. We then

calculate the transition rates by converting the discrete Markov process into a continuous one using the sampling timestep.

a. *H-bond Survival Time*

In the main text, we use the Markov model to calculate an approximate H-bond breaking rate, W_{break},

$$W_{\text{break}} \approx W_{\text{full}\to\text{top}} + W_{\text{full}\to\text{bottom}}, \tag{57}$$

One could argue that other processes should contribute to this:

$$W_{\text{break}} \approx W_{\text{full}\to\text{top}} + W_{\text{full}\to\text{bottom}} + W_{\text{full}\to\text{empty}} + W_{\text{top}\to\text{empty}} + W_{\text{bottom}\to\text{empty}}. \tag{58}$$

This is a moot point for two reasons: First, the empty state is rare, so the transition probabilities to it are negligibly small. Second, these rates follow the same trend anyways.

To verify that W_{break} is a good proxy for the H-bond breaking rate, we calculate the survival time of an H-bond between two molecules in the pore explicitly, by defining an H-bond as an O-O separation of 3.5 Å or less and a O-H-O angle of 30° or less [37]. We then calculate the average time that an H-bond lasts between two molecules inside the pore. We ignore H-bonds which "break" because one of the molecules leaves the pore. This gives a true estimate of the H-bond survival time, which is not influenced by any transport events. We find that this survival time follows the same trend as W_{break}, so we conclude that the Markov estimate of the H-bond breaking rate accurately captures the H-bond dynamics. If the survival time is converted to a breaking rate ($W_{\text{break}} = \tau^{-1}$), we get the same order of magnitude: this estimate ranges from about 2 to 3.5 ps^{-1}, while the Markov estimate ranges from about 0.9 to 1.2 ps^{-1}.

XI. REYNOLDS NUMBER CALCULATIONS

The Reynolds number (Re) is

$$\text{Re} = \frac{u_{\text{in}} L \rho_0}{\eta}, \tag{59}$$

where u_{in} is the velocity of the fluid inside the pore, L is the length of the pore, ρ_0 is the bulk density of the fluid, and η is the bulk viscosity of the fluid. It is clear that the velocity of the fluid is higher inside the pore than in the

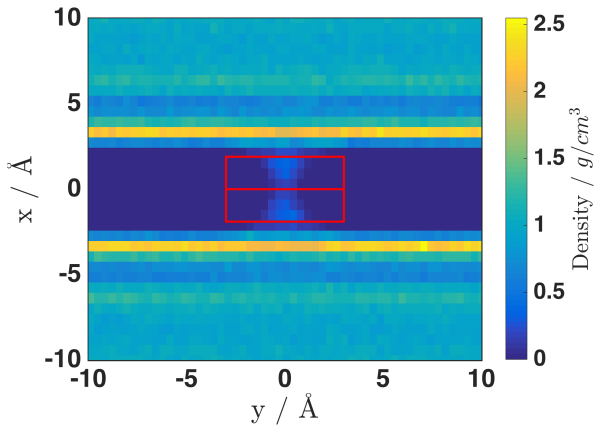

FIG. 5. The water density as a function of x, the direction of flow, and y, one of the other two dimensions. The red boxes are used to define the Markov states, as discussed in the text.

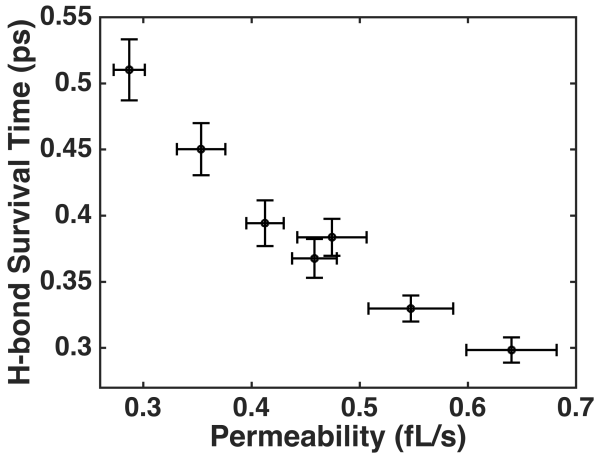

FIG. 6. The survival time of an H-bond between two water molecules in the pore, calculated using an explicit definition of an H-bond, as discussed in the text. The survival time is anti-correlated with the permeability, meaning that the breaking rate is correlated with the permeability. This supports the data in Fig. 3b in the main text.

bulk. Geometrical arguments suggest that

$$u_{\text{in}} = \frac{JL_y}{d\rho_0}, \tag{60}$$

and this is supported empirically. Using Eq. 59, we have

$$\text{Re} = \frac{JL_yL}{\eta d}. \tag{61}$$

To calculate Re, we need to know η. We measure the viscosity for a bulk 2D system with no channel at the relevant conditions of $T = 2\ \epsilon/k_B$, and $\rho_0 = 0.8\ \sigma^{-2}$ using the Green-Kubo relation [38],

$$\eta = \frac{1}{Vk_BT}\int_0^\infty dt\,\langle\sigma_{xy}(0)\sigma_{xy}(t)\rangle, \tag{62}$$

where σ_{xy} is the off-diagonal element of the 2D stress tensor, and V is the volume of the system (area in 2D). We find no evidence that this integral diverges as discussed in Refs. [39–41]; the autocorrelation function does not decay as t^{-1}, it decays as $\exp(-t)$. We also find no system size dependance of the viscosity for systems from $20 \times 20\ \sigma^2$ to $100 \times 100\ \sigma^2$. We find $\eta = 2.2 \pm 0.1\ \sqrt{m\epsilon}/\sigma$.

In the water simulations, we measure u_{in} explicitly in a GD simulation set at $q = 11$ molecules/ns,

$$u_{\text{in}} \approx 2 \times 10^{-5}\ \text{Å/fs}. \tag{63}$$

We use values of ρ_0 and η for SPC/E water from the literature: $\rho_0 = 0.998\ \text{g/cm}^3$ [27]; $\eta = 0.729$ mPa·s [42]. The "length" of the pore is described in Eq. 55. The result is $\text{Re} \approx 0.001$.

XII. VERY HIGH REYNOLDS NUMBER

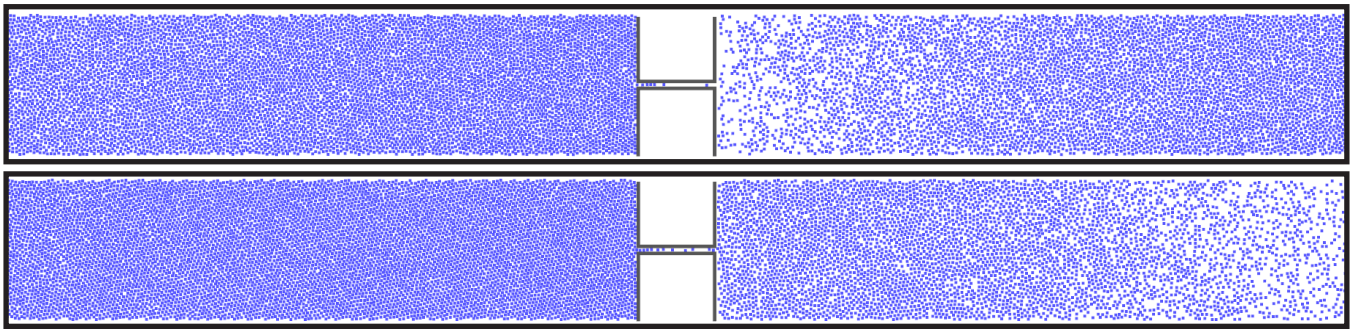

FIG. 7. Snapshots of Gaussian dynamics (top) and the pump method (bottom) at high Reynolds number. In Gaussian dynamics the density is minimum just past the channel, as would be expected. In the pump method, the density minimum is before the pump region. This is caused by the discontinuity in the density profile of the pump method (§ VII). This is simply a more extreme example of the discontinuity shown in § VII. Note that we made no effort to ensure that these simulations are at steady state or converged with respect to box length. This is purely illustrative. These results show that at high enough Re, the density minimum can qualitatively shift location. This is because the pump method enforces a discontinuity in the density at the onset of the pump region. It is possible that a long enough box would fix this issue, because the density would have enough space to relax naturally before being subjected to the pump region. If there is no deeper issue, there is still the practical point that the pump method requires longer boxes to equilibrate at high Re.

[1] Evans, D. J.; Morriss, G. *Statistical Mechanics of Nonequilibrium Liquids*, 2nd ed.; Cambridge University Press: Cambridge, 2008.
[2] Hoover, W. G.; Ladd, A. J. C.; Moran, B. *Phys. Rev. Lett.* **1982**, *48*, 1818–1820.
[3] Evans, D. J. *J. Chem. Phys.* **1983**, *78*, 3297–3302.
[4] Evans, D. J.; Hoover, W. G.; Failor, B. H.; Moran, B.; Ladd, A. J. C. *Phys. Rev. A* **1983**, *28*, 1016–1021.
[5] Edberg, R.; Evans, D. J.; Morriss, G. P. *J. Chem. Phys.* **1986**, *84*, 6933–6939.

[6] Morriss, G. P.; Evans, D. J. *Comput. Phys. Commun.* **1991**, *62*, 267–278.
[7] Nosé, S. *J. Chem. Phys.* **1984**, *81*, 511–519.
[8] Hoover, W. G. *Phys. Rev. A* **1985**, *31*, 1695–1697.
[9] Evans, D. J.; Morriss, G. P. *Phys. Rev. Lett.* **1986**, *56*, 2172–2175.
[10] Hagen, G. *Ann. Phys. (Leipzig)* **1839**, *122*, 423–442.
[11] Poiseuille, J. L. *Comptes rendus hebdomadaires des sances de l'Académie des Sciences* **1840**, *11*, 961 and 1041.
[12] Poiseuille, J. L. *Comptes rendus hebdomadaires des sances de l'Académie des Sciences* **1841**, *12*, 112.
[13] Bird, R. B.; Stewart, W. E.; Lightfoot, E. N. *Transport Phenomena*, 2nd ed.; John Wiley & Sons, Inc.: New York, 2006.
[14] Ashurst, W. T.; Hoover, W. G. *Phys. Rev. A* **1975**, *11*, 658–678.
[15] Heyes, D. M. *Physica A* **1985**, *133*, 473–496.
[16] Heyes, D. M. *J. Chem. Soc. Faraday Trans. 2* **1986**, *82*, 1365.
[17] Zhu, F.; Tajkhorshid, E.; Schulten, K. *Phys. Rev. Lett.* **2004**, *93*, 224501.
[18] Zhu, F.; Tajkhorshid, E.; Schulten, K. *Biophys. J.* **2002**, *83*, 154–160.
[19] Zhu, F.; Tajkhorshid, E.; Schulten, K. *Biophys. J.* **2004**, *86*, 50–57.
[20] Chandler, D.; Weeks, J. D. *Phys. Rev. Lett.* **1970**, *25*, 149–152.
[21] Weeks, J. D.; Chandler, D.; Andersen, H. C. *J. Chem. Phys.* **1971**, *54*, 5237–5247.
[22] Chandler, D.; Weeks, J. D.; Andersen, H. C. *Science* **1983**, *220*, 787–794.
[23] Huang, C.; Nandakumar, K.; Choi, P. Y. K.; Kostiuk, L. W. *J. Chem. Phys.* **2006**, *124*, 234701.
[24] Huang, C.; Choi, P. Y. K.; Kostiuk, L. W. *Phys. Chem. Chem. Phys.* **2011**, *13*, 20750.
[25] Turgman-Cohen, S.; Araque, J. C.; Hoek, E. M. V.; Escobedo, F. A. *Langmuir* **2013**, *29*, 12389–12399.
[26] Docherty, S. Y.; Nicholls, W. D.; Borg, M. K.; Lockerby, D. A.; Reese, J. M. *Proc. Inst. Mech. Eng. C.* **2014**, *228*, 186–195.
[27] Berendsen, H. J. C.; Grigera, J. R.; Straatsma, T. P. *J. Phys. Chem.* **1987**, *91*, 6269–6271.
[28] Ryckaert, J.-P.; Ciccotti, G.; Berendsen, H. J. C. *J. Comput. Phys.* **1977**, *23*, 327–341.
[29] Suk, M. E.; Aluru, N. R. *J. Phys. Chem. Lett.* **2010**, *1*, 1590–1594.
[30] Werder, T.; Walther, J. H.; Jaffe, R. L.; Halicioglu, T.; Koumoutsakos, P. *J. Phys. Chem. B* **2003**, *107*, 1345–1352.
[31] Ostrowski, J. H. J.; Eaves, J. D. *J. Phys. Chem. B* **2014**, *118*, 530–536.
[32] Taherian, F.; Marcon, V.; van der Vegt, N. F. A.; Leroy, F. *Langmuir* **2013**, *29*, 1457–1465.
[33] Shinoda, W.; Shiga, M.; Mikami, M. *Phys. Rev. B* **2004**, *69*, 134103.
[34] Hockney, R. W.; Eastwood, J. W. *Computer Simulation Using Particles*; Taylor & Francis: New York, 1989.
[35] Plimpton, S. *J. Comput. Phys.* **1995**, *117*, 1–19.
[36] Kampen, N. G. V. *Stochastic Processes in Physics and Chemistry*; Elsevier, 1992.
[37] Luzar, A.; Chandler, D. *Phys. Rev. Lett.* **1996**, *76*, 928–931.
[38] Frenkel, D.; Smit, B. *Understanding Molecular Simulation: From Algorithms to Applications*, 2nd ed.; Academic Press: San Diego, 2001.
[39] Alder, B. J.; Wainwright, T. E. *Phys. Rev. Lett.* **1967**, *18*, 988–990.
[40] Alder, B. J.; Wainwright, T. E. *Phys. Rev. A* **1970**, *1*, 18–21.
[41] Pomeau, Y.; Resibois, P. *Phys. Rep.* **1975**, *19*, 63–139.
[42] González, M. A.; Abascal, J. L. F. *J. Chem. Phys.* **2010**, *132*, 096101.